Available online at www.sciencedirect.com

SciVerse ScienceDirect

Acta Materialia 60 (2012) 2350–2358

Acta MATERIALIA

www.elsevier.com/locate/actamat

Prediction of thermal cross-slip stress in magnesium alloys from a geometric interaction model

Joseph A. Yasi [a], Louis G. Hector Jr. [b], Dallas R. Trinkle [c,*]

[a] Department of Physics, University of Illinois at Urbana–Champaign, Urbana, IL 61801, USA
[b] General Motors R&D Center, 30500 Mound Road, Warren, MI 48090, USA
[c] Department of Materials Science and Engineering, University of Illinois at Urbana–Champaign, Urbana, IL 61801, USA

Received 12 April 2011; received in revised form 10 November 2011; accepted 3 January 2012

Abstract

We develop a geometry-based model from first-principles data for the interaction of solutes with a prismatic screw dislocation core, and predict the thermally activated cross-slip stress above room temperature in Mg alloys. Electronic structure methods provide data for the change in prismatic stacking fault energy for different possible fault configurations for 29 different solutes. The direct solute–dislocation interaction energies for solutes that produce stable prismatic screw dislocation cores (K, Na, Sc and Ca) is correlated with stacking fault misfits. This geometric interaction model produces similar prediction errors for all 29 solutes. The model predicts alloys with cross-slip stresses lower than pure Mg for three previously considered solutes (K, Na and Sc) and three new solutes (Ca, Y and Zr). The model also qualitatively confirms the experimental observation that Mg–Li alloys have lower cross-slip stress than pure Mg. In particular, low concentrations of Y are predicted to significantly decrease the cross-slip stress in Mg.

Keywords: Magnesium alloys; Dislocations; Plastic deformation; Cross-slip; Density functional theory

1. Introduction

Expanding the use of the lightweight structural metal Mg—as a replacement for Al and steels in automotive applications [1]—requires the solution of a variety of metallurgical issues [2], including formability. Current Mg alloys require temperatures near 300 °C for forming (e.g. warm stamping) to activate the five independent slip systems required by the von Mises criterion [3]; this is in part due to the large anisotropy between basal and prismatic slip [4]. Cross-slip of *a*-type dislocations from the (0 0 0 1) basal plane onto the $(0\ 1\ \bar{1}\ 0)$ prismatic plane requires large stresses or high temperatures. Experimentally, few solutes have been found to lower the stress for cross-slip: Al and Zn lower the stress at low (below room) temperatures [5], while Li can lower the cross-slip stress in both regimes [6–9]. The difficulty of performing experiments to measure cross-slip stresses for alloys—requiring single-crystal samples oriented for prismatic slip—is compounded by the possibility that, like solid-solution softening in body-centered cubic (bcc) alloys [10], it may occur over a limited concentration and temperature range. Hence, we have developed new state-of-the-art first-principles predictions of solute–dislocation interactions coupled with computational modeling of thermally activated cross-slip in the presence of solutes to guide the design of new Mg alloys that can be formed at temperatures below 300 °C [11].

In previous work, we developed a numerical model (and analytic approximation) to predict basal to prismatic cross-slip stress in Mg in the presence of solutes from density-functional theory (DFT) dislocation–solute interaction data [11]. The results were limited to solutes that would not destabilize the prismatic screw dislocation core after substitution. Despite this limitation, three binary alloys—Mg–K, Mg–Na and Mg–Sc—were predicted to lower the

* Corresponding author.
E-mail address: dtrinkle@illinois.edu (D.R. Trinkle).

1359-6454/$36.00
doi:10.1016/j.actamat.2012.01.004

thermally activated cross-slip stress. The thermal cross-slip model was based on changes in prismatic kink energies in the presence of a random field of solutes; the double-kink nucleation model is valid above room temperature up to approximately 700 K. The model [11] has been validated both by comparing the mechanism against *in situ* characterization of cross-slip [12–14] in this temperature regime and the measurement of single-crystal cross-slip stress with temperature [15]. Prismatic kinks must nucleate, separate and propagate along the line in the presence of a random field of solutes; the solutes produce distributions of enthalpy barriers for these processes. The solute distribution is assumed to be random to describe the flow of dislocations after breaking away from any kind of initial solute field, but excluding solute drag. The effect of multiple solutes is considered to be additive, and solute–solute interaction energies which could produce short-range ordering of the solutes is ignored. This model has analytic dilute-limit predictions of changes in cross-slip stress as well as non-dilute predictions.

The previous predictions required that solutes not destabilize the prismatic core to compute an interaction energy; however, other solutes may reduce the stress for cross-slip as long as the energy of solutes in a prismatic core was reduced relative to the same site in the basal screw dislocation core. Here, we develop a geometry-based model for the interaction energy of solutes with a prismatic screw dislocation core that is optimized to reproduce direct interaction data [11]. This model allows the prediction of interactions with prismatic cores for 29 solutes (the same considered in an earlier study of basal strengthening [16]) whether the interaction is attractive or repulsive. Combined with our model for thermally activated cross-slip [11], we predict changes in cross-slip stress with temperature and concentration. Of the 29 solutes, six lower the cross-slip stress: Ca, K, Na, Sc, Y and Zr. The interaction of Li is weaker than the prediction error of our model, though it is consistent with experimental observations of softening. We connect the prismatic stacking fault geometry to the prismatic screw dislocation core geometry to quantitatively correlate changes in stacking fault energy to interaction energies, and hence predict the cross-slip stress of binary Mg alloys. Hence, we can predict new, more formable Mg alloys from solute misfit data.

2. Computational methodology

To model the interaction of solutes with the Mg prismatic screw dislocation core, solute interactions with the prismatic stacking faults were calculated within DFT using VASP [17,18]. We use a plane-wave basis set with the projector augmented-wave (PAW) method [19] with potentials generated by Kresse and Joubert [20]. The Perdew–Wang 91 generalized gradient approximation exchange–correlation potential [21] and a plane-wave kinetic energy cutoff of 273 eV for pure Mg ensures accurate treatment of the potentials. Plane-wave cutoffs and electronic configurations for the PAW potentials for solutes in Mg are provided in Table 1. To calculate the chemical misfits for solute X in Eq. (1), we calculate stacking faults with a $5\sqrt{3}a \times 2a \times 2c$ (Mg_{79}–X_1) supercell and a $1 \times 17 \times 16$ k-point mesh with a Methfessel–Paxton smearing of 0.5 eV; atoms are relaxed normal to the fault plane to within 5 meV Å^{-1}, for an energy accuracy of 5 meV. Energies of individual Mg atoms at different planes in the stacking fault (see below) are also computed with an embedded atom method (EAM) potential [22]; it has been validated with basal and prismatic screw dislocation core structures and stacking fault energies in Mg [23]. The screw dislocation core geometries with Burgers vector $\vec{b} = \frac{a}{3}[2\,\bar{1}\,\bar{1}\,0]$ have previously been calculated for the basal geometry [23] and prismatic geometry [11].

3. Results

Fig. 1 shows the possible prismatic $(0\,1\,\bar{1}\,0)$ stacking fault geometries and energies in magnesium from PAW and EAM. The prismatic plane is corrugated, with two possible choices of cut plane for the stacking fault, "easy" and "hard," with unrelaxed planar separations $\frac{a}{\sqrt{3}}$ and $\frac{a}{2\sqrt{3}}$, respectively. Atoms across the fault plane are displaced by $b/2 = \frac{a}{6}[2\,\bar{1}\,\bar{1}\,0]$ relative to their bulk positions to form an unstable stacking fault. The hard stacking fault is more than twice the energy of the easy stacking fault at the $\frac{a}{6}[2\,\bar{1}\,\bar{1}\,0]$; this is due to the displacement of twice the number of nearest-neighbor bonds relative to the easy fault. Inside of the prismatic screw dislocation core, displacements corresponding to both faults appear. Moreover, there are two possible sites for solute substitution, and similarly, both geometries appear in the prismatic screw dislocation core. The EAM calculations agree well with the PAW potential. In addition, the EAM potential provides information about the partitioning of energy between the two planes: the energy change for a Mg atom in the easy fault is $E_{\text{E1}}^{\text{Mg-prism}} = 74$ meV for the first plane and $E_{\text{E2}}^{\text{Mg-prism}} = 54$ meV for the second compared to bulk; while for the hard fault, the Mg atom energy is $E_{\text{H1}}^{\text{Mg-prism}} = 205$ meV for the first plane and $E_{\text{H2}}^{\text{Mg-prism}} = 23$ meV for the second compared to bulk. This energy is not known from DFT, only the total fault energy. We use these changes to determine what fraction of the stacking fault energy change is due to a solute.

Table 1 gives the solute misfits—changes in stacking fault energies—for 29 different substitutional solutes in Mg. To predict the solute energies in the prismatic core, we need to know how the stacking fault displacements change the energy of solute compared with bulk. For each solute, we compute the energy with the solute in the bulk and in each of the two planes for each fault, with relaxation normal to the fault plane. We then subtract the energy of the remaining Mg atoms in both planes of the fault, so that only the change in energy of the solute atom remains. This subtraction is equivalent to subtracting off the total fault energy without a solute and adding in the energy for a Mg atom at the substitutional site. Finally, we scale the

Table 1
Solute misfits in Mg from DFT. Misfits are defined as fractional change of site energy for a solute in a fault (cf. Eqn. (1)). We compute six different unitless misfits: easy prismatic stacking fault energy for solutes in the first (ε_{E1}) and second (ε_{E2}) planes from the fault; hard prismatic stacking fault energy for solutes in the first (ε_{H1}) and second (ε_{H2}) planes from the fault; and from Ref. [16], basal stacking fault energy for solutes in the slip plane (ε_{SFE}) and size misfit (ε_b). The PAW valence configuration and energy cutoff are also listed. Solutes marked by an asterisk (*) lead to a stable prismatic core, and are used to fit the solute–dislocation interaction model.

	PAWPP	Cutoff	ε_{E1}	ε_{E2}	ε_{H1}	ε_{H2}	ε_{SFE}	ε_b
Ag	$[Kr]4d^{10}5s^1$	325 eV	1.172	−0.223	0.184	0.211	1.93	−0.171
Al	$[Ne]3s^23p^1$	313	0.843	−0.187	0.165	0.043	−1.25	−0.115
As	$([Ar]3d^{10})4s^24p^3$	273	0.415	−1.325	−0.697	−0.099	−3.60	−0.145
Be	$[He]2s^2$	390	1.137	−0.647	0.032	0.124	1.34	−0.252
Bi	$([Xe]4f^{14}5d^{10})6s^26p^3$	273	0.014	−0.701	−0.416	−0.102	−4.45	0.162
Ca*	$[Ar]4s^2$	273	−1.554	0.633	0.711	−0.304	−1.39	0.282
Cd	$[Kr]4d^{10}5s^2$	357	0.771	−0.121	0.130	0.100	−0.06	−0.046
Ga	$([Ar]3d^{10})4s^24p^1$	273	0.733	−0.426	−0.006	0.012	−1.09	−0.119
Ge	$([Ar]3d^{10})4s^24p^2$	273	0.753	−0.740	−0.230	0.002	−2.04	−0.139
Hg	$([Xe]4f^{14})5d^{10}6s^2$	303	0.793	−0.408	−0.063	0.062	−0.18	−0.073
In	$([Kr]4d^{10})5s^25p^1$	273	0.408	−0.257	0.021	−0.017	−1.58	0.028
Ir	$([Xe]4f^{14})5d^86s^1$	274	2.324	0.096	0.914	0.544	4.33	−0.435
K*	$[Mg]3p^64s^1$	273	−1.717	−0.207	−0.195	−0.474	−3.38	0.425
Li	$[He]2s^1$	273	0.422	0.209	0.408	0.107	1.89	−0.058
Mn	$[Ar]3d^64s^1$	351	1.683	0.720	1.241	0.415	2.12	−0.356
Na*	$[Ne]3s^1$	273	−0.371	0.156	0.253	−0.074	0.29	0.126
Pb	$([Xe]4f^{14}5d^{10})6s^26p^2$	273	0.033	−0.446	−0.177	−0.069	−3.00	0.132
Pd	$[Kr]4d^95s^1$	326	1.596	−0.283	0.404	0.374	3.75	−0.318
Pt	$([Xe]4f^{14})5d^96s^1$	299	1.704	−0.508	0.336	0.378	3.39	−0.377
Ru	$[Kr]4d^75s^1$	277	2.280	0.708	1.379	0.595	3.92	−0.401
Sb	$([Kr]4d^{10})5s^25p^3$	273	0.329	−0.845	−0.498	−0.110	−4.65	0.046
Sc*	$[Ar]3d^24s^1$	273	−0.510	1.278	1.343	−0.038	−1.20	0.035
Si	$[Ne]3s^23p^2$	319	0.825	−0.903	−0.276	−0.002	−2.03	−0.199
Sn	$([Kr]4d^{10})5s^25p^2$	273	0.372	−0.485	−0.164	−0.052	−3.08	0.037
Ti	$[Ar]3d^34s^1$	273	0.355	1.412	1.495	0.141	−0.81	−0.149
Tl	$([Xe]4f^{14}5d^{10})6s^26p^1$	273	0.201	−0.359	−0.109	−0.048	−1.61	0.047
Y	$([Ar]3d^{10})4s^24p^64d^15s^2$	275	−1.596	1.240	1.332	−0.262	−1.70	0.212
Zn	$[Ar]3d^{10}4s^2$	360	0.910	−0.354	0.061	0.079	0.32	−0.153
Zr	$[Kr]4d^35s^1$	273	−0.444	1.709	1.777	0.052	−1.27	−0.038

solute energy by the total fault energy to define a unitless "misfit" for solute X in fault $f=(E,H)$ in plane $p=(1,2)$ as:

$$\varepsilon_{fp}(\mathrm{X})=\frac{E_{fp}(\mathrm{Mg_{79}X_1})-E_{\mathrm{bulk}}(\mathrm{Mg_{79}X_1})-4ca\gamma_f+E_{fp}^{\text{Mg-prism}}}{ca\gamma_f} \tag{1}$$

for lattice constants a and c and fault energy γ_f. In addition to this data from the prismatic faults, we use two misfits for the basal core interaction: solute-induced changes to the basal stacking fault energy (the "chemical misfit" ε_{SFE}) and lattice constant (the "size misfit" ε_b) calculated in Ref. [16]. Of the 29 solutes we computed, only six show a reduction in the prismatic easy fault energy ($\varepsilon_{E1}<0$) and these same solutes will lead to significant softening: Ca, K, Na, Sc, Y and Zr. Li raises the prismatic stacking fault energy much less than it raises the basal stacking fault energy; this leads to a reduction in cross-slip stress.

Fig. 2 shows the correlation among the prismatic stacking fault misfit data, which suggests that the solutes considered can be well described with only two degrees of freedom. Strong correlations are seen between ε_{E1} and ε_{H2}, ε_{E2} and ε_{H1}, and a weaker correlation between ε_{H1} and ε_{H2}. This is captured in the scaled, uncentered covariance matrix $\langle\varepsilon_{fp}\varepsilon_{f'p'}\rangle\Big/\sqrt{\langle\varepsilon_{fp}^2\rangle\langle\varepsilon_{f'p'}^2\rangle}$:

	ε_{E1}	ε_{E2}	ε_{H1}	ε_{H2}
ε_{E1}	1	−0.272	0.186	0.899
ε_{E2}	−0.272	1	0.825	0.092
ε_{H1}	0.186	0.825	1	0.429
ε_{H2}	0.899	0.092	0.429	1

(2)

Fig. 2 is the data corresponding to the lower triangle of this matrix. The correlation is important as sites in the prismatic screw dislocation core will have a combination of ε_{E1} and ε_{H2} geometry, or ε_{E2} and ε_{H1} geometry. We

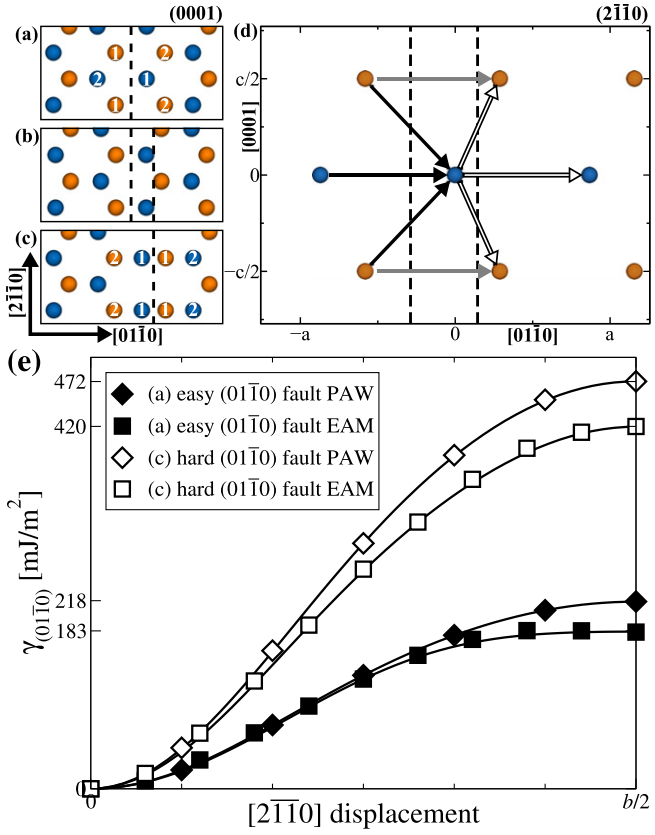

Fig. 1. Prismatic $(0\,1\,\bar{1}\,0)$ stacking fault geometries and energies in Mg from PAW and EAM. The prismatic stacking fault displaced along the $[2\,\bar{1}\,\bar{1}\,0]$ direction can be in an (a) easy or (c) hard configuration relative to (b) bulk depending on the placement of the slip plane (dashed lines). The easy fault has an unrelaxed planar separation of $\frac{a}{\sqrt{3}}$ compared with $\frac{a}{2\sqrt{3}}$ for the hard fault. The labels 1 and 2 in the faults correspond to distances from the fault plane, while orange and blue atoms are on alternating basal planes. Rotating the view (a)–(c) to the $(2\,\bar{1}\,\bar{1}\,0)$ plane shows the (d) differential displacements as arrows corresponding to the total relative displacement of atomic rows. Black and gray arrows are for the easy fault, and white and gray arrows are for the hard fault; this corresponds to the differential displacements in Fig. 3. Finally, the (e) generalized stacking fault energy for each fault shows no stable point in the displaced direction, with a fault energy of 218 mJ m^{-2} for the easy fault and 472 mJ m^{-2} for the hard fault from PAW, and 183 and 420 mJ m^{-2} from EAM.

correlate site energies for different solutes in a prismatic core with prismatic misfits. The four solutes whose direct prismatic core interaction is known (K, Na, Sc and Ca) also show similar correlations to the other solutes.

The strong correlation between different misfits for a range of solutes is also reflected in the local changes in electronic structure for Mg without solute substitution. We computed the projected electronic density of states (DOS) for Mg atoms in the hexagonal close-packed (hcp) crystal structure, and in two sites each in the easy and hard prismatic stacking faults. For Mg, only s and p contributions arise; Fig. 4 shows that most of the changes occur near the Fermi energy E_F. To quantitatively compare the four different possible solute substitutional sites, we compute the overlap of two DOS differences from the bulk: let $n_0(E)$ be the DOS for the hcp sites, and $n_1(E)$ and $n_2(E)$ DOS for two different sites, then the scaled DOS overlap N_{ij} is:

$$N_{ij} = \frac{\int_{-\infty}^{E_F}(n_i(E)-n_0(E))(n_j(E)-n_0(E))dE}{\left[\int_{-\infty}^{E_F}(n_i(E)-n_0(E))^2\,dE\cdot\int_{-\infty}^{E_F}(n_j(E)-n_0(E))^2\,dE\right]^{1/2}} \tag{3}$$

Eq. (3) is computed for s and p densities separately, and shows a very similar structure to Eq. (2):

$$N^{(s)} = \begin{array}{c|cccc} & \text{E1} & \text{E2} & \text{H1} & \text{H2} \\ \text{E1} & 1 & 0.618 & 0.519 & 0.866 \\ \text{E2} & 0.618 & 1 & 0.866 & 0.798 \\ \text{H1} & 0.519 & 0.866 & 1 & 0.628 \\ \text{H2} & 0.866 & 0.798 & 0.628 & 1 \end{array} \tag{4}$$

$$N^{(p)} = \begin{array}{c|cccc} & \text{E1} & \text{E2} & \text{H1} & \text{H2} \\ \text{E1} & 1 & -0.128 & -0.084 & 0.916 \\ \text{E2} & -0.128 & 1 & 0.974 & 0.001 \\ \text{H1} & 0.084 & 0.974 & 1 & 0.063 \\ \text{H2} & 0.916 & 0.001 & 0.063 & 1 \end{array} \tag{5}$$

with the strongest similarity in the changes in p density of states. This is not surprising; the main difference then in the electronic structure of the stacking fault regions is in the distortion of p-type angular bonding. This also clearly connects the different responses of solutes to the bonding environment before solutes are even introduced into the calculation.

Fig. 3 shows the differential displacements along the screw direction of the metastable prismatic screw dislocation core and the stable basal screw dislocation core from DFT; the interaction parameters y_i are discussed later. The prismatic core differential displacements are labeled whether they correspond to easy or hard prismatic faults, or are common to both. The differential displacements are largest for eight core sites, corresponding to two partials: one leading (ℓ) and the other trailing (t) relative to the transformation from a basal dislocation core. Numbering the sites based on their distance from the center, the 1 and 3 sites have large easy-prismatic displacements relative to their nearest neighbors (corresponding to ε_{E1}), while 2 and 4 sites have large hard-prismatic displacements relative to their nearest neighbors (corresponding to ε_{H1}). Each 1 site neighbors a 2 site across the fault plane, and each 3 site neighbors a 4 site across the fault plane; hence, the 1 and 3 sites are in the second plane for a hard fault (ε_{H2}), and the 2 and 4 sites are in the second plane for an easy fault (ε_{E2}). We require information about both planes in both faults and due to the strong correlation between fault misfits (Eq. (2)), we expect to be able to predictively model interaction energies with the available data. Unfortunately, due to the complexity of the local displacements, the most accurate approach is to parametrize an interaction model based on direct interaction data from Ref. [11]. For the basal screw dislocation core, the largest differential

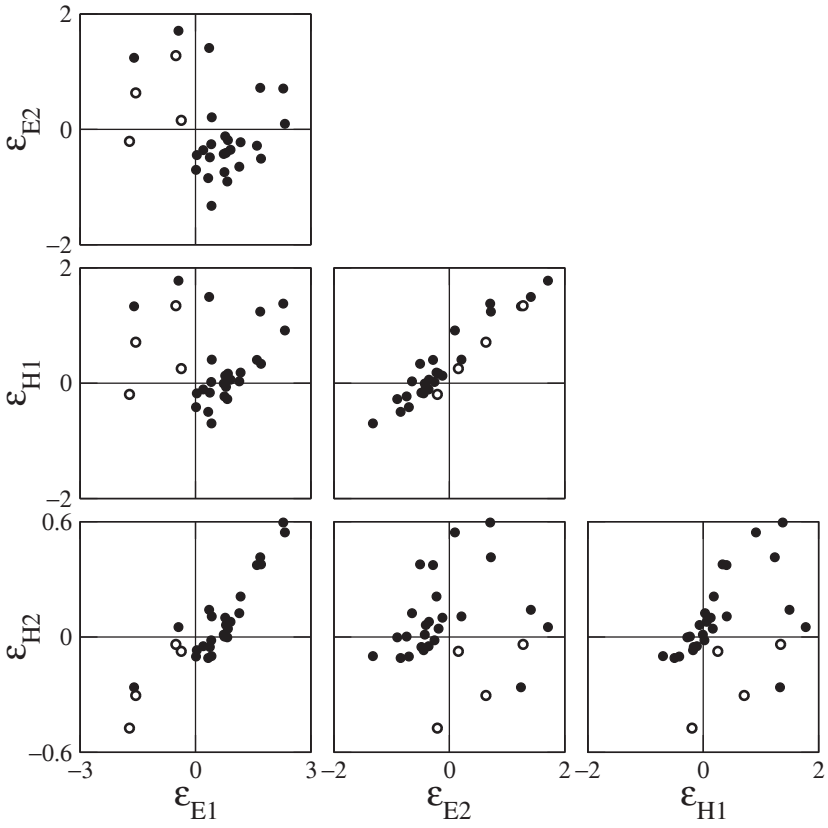

Fig. 2. Prismatic stacking fault misfits in Table 1 showing correlation between ε_{E1} and ε_{H2}, ε_{E2} and ε_{H1}, and a weaker correlation between ε_{H1} and ε_{H2}; cf. Eqn. (2). Open symbols are Ca, K, Na and Sc, which are used to fit the geometric model; and filled symbols are the remaining 25 solute elements. The presence of strong correlation among two pairs of misfits in the solute data suggests that, for the solutes considered here, only two degrees of freedom are contained in the misfit data.

displacements correspond to basal slip, with volumetric strain near the cores [16]; hence, the interaction energy is modeled from basal stacking fault energy changes ε_{SFE} and size misfit ε_b. The site interaction energies for the prismatic and basal screw dislocation core are included in Fig. 3, given by Eqs. (8), (9) and (11) derived below.

Fig. 4 shows the local projected DOS for Mg in hcp, in different prismatic stacking fault sites as well as in the four different dislocation core environments. From the geometry, we expect information from the different fault configurations to be useful, but in addition, we can quantify the correlation of changes in DOS at the different core sites to the different prismatic stacking faults. From the geometry, we expect sites 1 and 3 to correlate with E1 and H2 faults, and 2 and 4 to correlate with E2 and H1. The DOS overlaps of Eq. (3) for the core sites are:

$$N^{(s)} = \begin{array}{c|cccc} & \text{E1} & \text{E2} & \text{H1} & \text{H2} \\ \text{core 1} & 0.977 & 0.678 & 0.520 & 0.930 \\ \text{core 2} & 0.282 & 0.894 & 0.707 & 0.626 \\ \text{core 3} & 0.963 & 0.684 & 0.529 & 0.918 \\ \text{core 4} & 0.763 & 0.950 & 0.763 & 0.906 \end{array} \quad (6)$$

$$N^{(p)} = \begin{array}{c|cccc} & \text{E1} & \text{E2} & \text{H1} & \text{H2} \\ \text{core 1} & 0.984 & -0.011 & 0.011 & 0.915 \\ \text{core 2} & -0.406 & 0.950 & 0.895 & -0.259 \\ \text{core 3} & 0.962 & 0.087 & 0.098 & 0.896 \\ \text{core 4} & 0.160 & 0.939 & 0.897 & 0.255 \end{array} \quad (7)$$

The correlation of changes in density of states is also reflected in the interaction model that we fit; these responses—before the substitution of solutes—provide a physical basis for our geometric interaction model.

The direct interaction energy data for solutes substituted into prismatic screw dislocation cores [11] is used to fit a site energy model that is a linear combination of solute misfit data. Of the six solutes that lead to a decrease in easy prismatic stacking fault energy, only four—Ca, K, Na and Sc—do not destabilize the metastable prismatic screw dislocation core when substituted into the core. The prismatic core is only stable for Ca at sites 1, 3 and 4, and Sc at sites 1, 2 and 3. The direct interaction energies are $E_i^{\text{prism}}(\text{X})$ for X = Ca, K, Na and Sc. The lack of other stable prismatic cores with solutes does not mean, however, that other solutes cannot lead to softening. Rather, it is

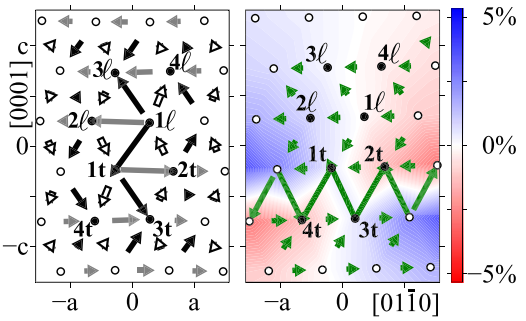

site i	$y_i^{\text{pr1.E1}}$	$y_i^{\text{pr1.H2}}$	$y_i^{\text{pr2.E1}}$	$y_i^{\text{pr2.H1}}$	$y_i^{\text{basal.SFE}}$	$y_i^{\text{basal.b}}$
4ℓ	11.74	61.28	26.33	7.19	2.296	36.48
3ℓ	114.9	–209.4	68.86	–27.53	2.055	–36.29
2ℓ	–7.77	87.62	11.13	12.63	4.005	–133.9
1ℓ	107.6	–145.0	75.35	–19.19	4.072	8.91
1t	107.6	–145.0	75.35	–19.19	15.55	–73.50
2t	–7.77	87.62	11.13	12.63	16.74	190.8
3t	114.9	–209.4	68.86	–27.53	15.64	–76.42
4t	11.74	61.28	26.33	7.19	16.81	189.7

Fig. 3. Differential displacement map of the relaxed Mg prismatic (left) and basal (right) screw dislocation cores from DFT, and corresponding interaction energy parameters (y_i) in meV. Arrows between two rows shows the differential displacement along the $\frac{a}{3}[2\,\bar{1}\,\bar{1}\,0]$ screw axis, up to a displacement of $b/2$. For the prismatic core, the arrow color identifies if the displacement is specific to an easy (black) or hard (white) fault, or both faults (gray); cf. Fig. 1. For the basal core, the green differential displacements are for the basal stacking fault and the background color shows atomic volumetric strain that is compressive (red) or tensile (blue). The solute interaction is computed at the eight labeled sites as the basal core transforms into the prismatic core; 1–4 go from the center of the prismatic core outward, with ℓ for the leading prismatic partial and t for the trailing prismatic partial. The leading and trailing partial sites are equal by symmetry. In the basal core, sites $1t$ and $3t$ are identical, as are $2t$ and $4t$. The optimized interaction parameters y_i for each site i reflect this; in addition, the prismatic interaction is weaker further from the core, and the basal interactions are weaker at the leading sites (away from the basal core) than the trailing sites (in the basal core). (For interpretation of the references to color in this figure legend, the reader is referred to the web version of this article.)

the energy difference between a solute site in the prismatic screw dislocation core and the basal core that affects the double-kink nucleation energy. To compute the energy of a solute at a site in the prismatic core, we fit a model for the site energies that is linear in two misfits. As Fig. 2 shows, there is a strong correlation among the misfits, and so only two misfits should be needed for a predictive fit. We considered all six possible pairings, and found that a fit of the energy for solute X to $E_i^{\text{prism}}(\text{X})$ based on ε_{E1} and ε_{H2}

$$E_i^{\text{pr1}}(\text{X}) = y_i^{\text{pr1.E1}}\varepsilon_{\text{E1}}(\text{X}) + y_i^{\text{pr1.H2}}\varepsilon_{\text{H2}}(\text{X}) \tag{8}$$

had the lowest RMS error (9.5 meV), while a fit of the energy from ε_{E1} and ε_{H1}

$$E_i^{\text{pr2}}(\text{X}) = y_i^{\text{pr2.E1}}\varepsilon_{\text{E1}}(\text{X}) + y_i^{\text{pr2.H1}}\varepsilon_{\text{H1}}(\text{X}) \tag{9}$$

had the second lowest error (10.8 meV). Note that while ε_{E1} appears in both fits, the parameters describing the interaction $y_i^{\text{pr1.E1}}$ and $y_i^{\text{pr2.E1}}$ in the two fits are different. The performance

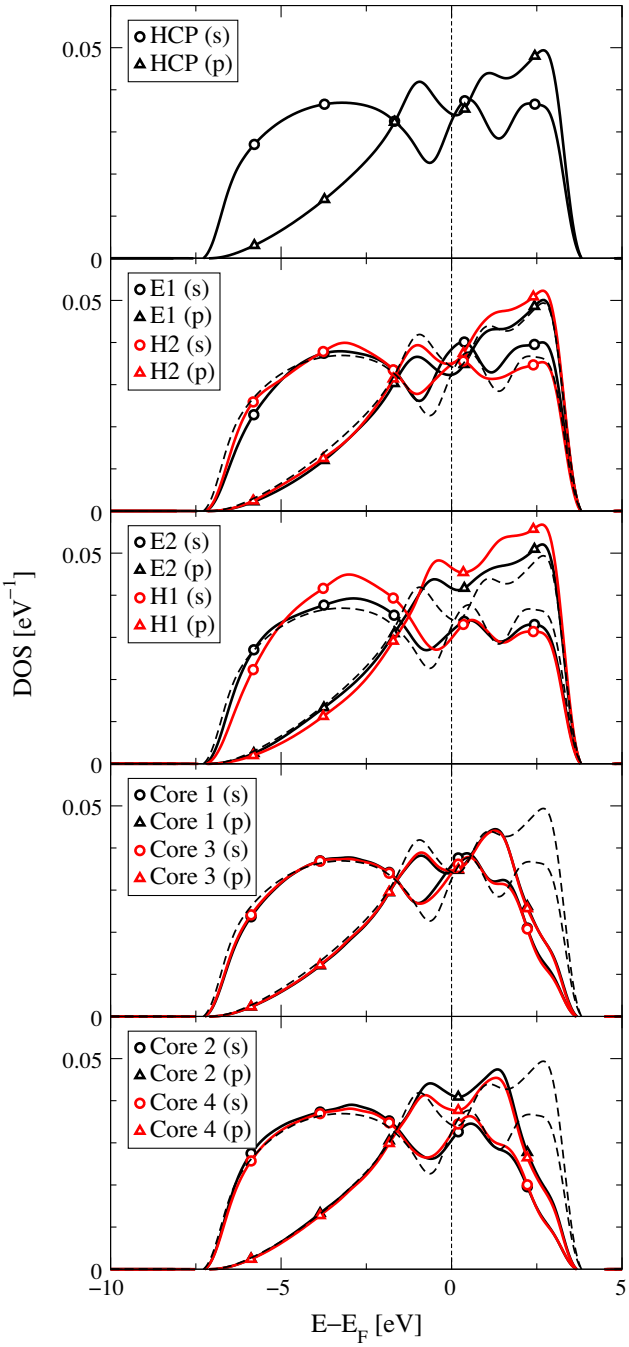

Fig. 4. Projected electronic density of states (DOS) for hcp Mg, in the four different prismatic stacking fault sites (E1 and H2, E2 and H1; cf. Fig. 1) and four prismatic screw dislocation core sites (1 and 3, 2 and 4; cf. Fig. 3). The dashed lines show the hcp site DOS for comparison with the defect sites. The common sites are grouped based on the strongest correlation to show the similarity between the electronic structure in the different defect sites; this similarity is mirrored in the geometry and solute interactions.

of the first fit is initially surprising as ε_{E1} and ε_{H2} are highly correlated, but the fit takes advantage of the correlation between ε_{H2} and ε_{H1}. While the two possible linear fits are able to accurately reproduce the direct interaction data, the difference in Eqs. (8) and (9) for the 25 solutes not in the fit was significantly larger than the RMS error of 10 meV. To

alleviate this shortcoming, we construct a robust fit: a simultaneous fit of Eqs. (8) and (9) constrained to produce similar prediction variability for all solutes—those included in the fit, and those not.

Fig. 3 lists the interaction energy data y_i^{pr1} and y_i^{pr2} for the robust fit of the prismatic screw dislocation core sites and y_i^{basal} for the basal screw dislocation core sites. We use linear least squares optimization of Eqs. (8) and (9) simultaneously with an additional penalty function to minimize the discrepancy between the model predictions for solutes not in the fit. This gives a mean-squared error χ^2_{error} to minimize against fit data $E_i^{\mathrm{prism}}(\mathrm{X})$:

$$\begin{aligned}\chi^2_{\mathrm{error}} = &\sum_{i,\mathrm{X}\in\mathrm{fit}} \left(E_i^{\mathrm{prism}}(\mathrm{X}) - E_i^{\mathrm{pr1}}(\mathrm{X})\right)^2 \\ &+ \sum_{i,\mathrm{X}\in\mathrm{fit}} \left(E_i^{\mathrm{prism}}(\mathrm{X}) - E_i^{\mathrm{pr2}}(\mathrm{X})\right)^2 \\ &+ \lambda \sum_{i,\mathrm{X}\in\mathrm{all}} \left(E_i^{\mathrm{pr1}}(\mathrm{X}) - E_i^{\mathrm{pr2}}(\mathrm{X})\right)^2 \end{aligned} \tag{10}$$

where λ is a parameter to be determined. The first two terms are the fit errors for Eqs. (8) and (9), while the last term is the prediction error for all solutes estimated as the difference between the two models. For any value of λ, the optimal pairs of $y_i^{\mathrm{pr1.E1}}$ and $y_i^{\mathrm{pr1.H2}}$, and $y_i^{\mathrm{pr2.E1}}$ and $y_i^{\mathrm{pr2.H1}}$ can be found. We select λ such that the RMS prediction errors match the RMS fit errors; overall, this gives us an RMS error of 14 meV for all solutes. The site energies—the average of Eqs. (8) and (9)—can then be used for each solute to predict changes in the basal-to-prismatic kink energy after subtracting the basal interaction energy [16]:

$$E_i^{\mathrm{basal}}(\mathrm{X}) = y_i^{\mathrm{basal.SFE}}\varepsilon_{\mathrm{SFE}}(\mathrm{X}) + y_i^{\mathrm{basal.b}}\varepsilon_b(\mathrm{X}) \tag{11}$$

and hence, the change in kink formation energy for a solute X at site i is:

$$\Delta E_i(\mathrm{X}) = \frac{1}{2}\left(E_i^{\mathrm{pr1}}(\mathrm{X}) + E_i^{\mathrm{pr2}}(\mathrm{X})\right) - E_i^{\mathrm{basal}}(\mathrm{X}) \tag{12}$$

with parameters in Fig. 3, and an expected error of 14 meV.

Table 2 shows the interaction statistics and strength parameters for 29 different substitutional solutes in Mg. The site energies are used in the double-kink nucleation and kink-migration interaction model for a random solution [11]; there, it was also shown that analytic expressions are possible for the limit of small solute concentration c_s. Briefly, we compute distributions of double-kink nucleation energies and migration barriers in order to obtain statistical averages for the thermally activated cross-slip process. The parameters that enter the analytic strengthening and softening equations are the mean value of interaction $\overline{\Delta E}$, the standard deviation δE, and the root mean squared interaction, $(\delta E^2 + \overline{\Delta E}^2)^{1/2}$. From these, the double-kink softening potency P_{dk} is:

$$P_{\mathrm{dk}} = \left(\frac{H^0_{\mathrm{dk}}}{2E_{\mathrm{f}}}4S\right)\left[\exp\left(-\frac{\overline{\Delta E}}{H^0_{\mathrm{dk}}} + \frac{1}{2}\left(\frac{\delta E}{H^0_{\mathrm{dk}}}\right)^2\right) - 1\right] \tag{13}$$

Table 2
Average and standard deviation of solute interaction energies from basal to prismatic screw dislocation cores, and unitless analytic strength parameters. The solute interactions are computed by combining the solute data from Table 1 with the interaction parameters y_i in Fig. 3 and Eq. (12); the average and standard deviation over the eight core sites are used to compute strength parameters for the simplified analytic model. Six solutes have positive P_{dk}, suggesting softening of cross-slip: Ca, K, Na, Sc, Y and Zr. Li has a small interaction energy, which makes its prediction less reliable than the others. Larger ratios $\chi = P_{\mathrm{dk}}/(\tau_{\mathrm{ath}}/\tau^\star)$ provide more reduction in the thermal cross-slip stress [11].

	Interaction [meV]			Strength parameter		
	$\overline{\Delta E}$	δE	$(\delta E^2 + \overline{\Delta E}^2)^{1/2}$	P_{dk}	$\tau_{\mathrm{ath}}/\tau^\star$	χ
Ag	37.4	32.4	49.4	−10.8	4.8	−2.3
Al	54.9	31.5	63.3	−15.4	6.1	−2.5
As	62.7	41.1	75.0	−15.8	7.2	−2.2
Be	45.2	37.2	58.5	−12.2	5.6	−2.2
Bi	45.5	33.9	56.8	−12.8	5.5	−2.3
Ca	**−64.1**	**48.1**	**80.1**	**80.4**	**7.7**	**10.4**
Cd	37.5	24.1	44.6	−11.9	4.3	−2.8
Ga	49.2	30.1	57.7	−14.2	5.6	−2.6
Ge	60.6	36.3	70.6	−16.0	6.8	−2.4
Hg	41.8	28.4	50.5	−12.6	4.9	−2.6
In	36.1	22.3	42.5	−11.7	4.1	−2.9
Ir	65.5	57.0	86.8	−13.6	8.4	−1.6
K	**−47.8**	**47.0**	**67.0**	**54.0**	**6.5**	**8.4**
Li	0.0	13.2	13.2	0.7	1.3	0.5
Mn	55.3	39.8	68.1	−14.4	6.6	−2.2
Na	**−22.3**	**16.0**	**27.5**	**13.9**	**2.7**	**5.3**
Pb	31.2	24.0	39.4	−10.1	3.8	−2.7
Pd	38.5	42.1	57.1	−9.3	5.5	−1.7
Pt	48.3	46.5	67.1	−11.4	6.5	−1.8
Ru	63.8	50.2	81.2	−14.6	7.8	−1.9
Sb	65.6	41.1	77.4	−16.4	7.5	−2.2
Sc	**−18.5**	**31.3**	**36.3**	**15.3**	**3.5**	**4.4**
Si	65.2	40.7	76.9	−16.4	7.4	−2.2
Sn	50.1	30.1	58.4	−14.4	5.6	−2.6
Ti	19.2	25.9	32.3	−5.8	3.1	−1.9
Tl	26.8	18.2	32.4	−9.3	3.1	−3.0
Y	**−65.6**	**57.2**	**87.1**	**97.9**	**8.4**	**11.7**
Zn	43.1	30.2	52.7	−12.7	5.1	−2.5
Zr	**−17.2**	**43.2**	**46.5**	**19.7**	**4.5**	**4.4**

and the athermal linear strengthening is:

$$\tau_{\mathrm{ath}}/\tau^\star = \frac{2}{\sqrt{e\pi}}\frac{2S_{\mathrm{c}}}{4b^3\tau^\star}\left(\delta E^2 + \overline{\Delta E}^2\right)^{1/2} \tag{14}$$

where the kink formation energy $E_{\mathrm{f}} = 515$ meV, double-kink formation energy scaled by strain-rate $H^0_{\mathrm{dk}} = 62.5$ meV, number of prismatic core sites $S_{\mathrm{c}} = 8$, number of kink sites $S = 120$, Burgers vector $b = 0.319$ nm, and prismatic Peierls stress $\tau^\star = 140$ MPa are all found in Ref. [11]. A positive P_{dk} is required for softening to occur, and only six solutes have $P_{\mathrm{dk}} > 0$: Ca, K, Na, Sc, Y and Zr. Li has a weak interaction which is susceptible to numerical errors (see below). For the analytic model, the cross-slip stress is the maximum of the double-kink limited stress:

$$\tau^{dk}(c_s) = \tau^{\star}\left(1-\alpha^0_{dk}\right)\left(1-\alpha^0_{dk}-\alpha^0_{dk}P_{dk}c_s\right) \quad (15)$$

where $\alpha^0_{dk} = k_B T/H^0_{dk}$; and the athermal hardening stress:

$$\tau^{a}(c_s) = \tau_{ath}c_s. \quad (16)$$

Both of these limiting forms are plotted as dashed and dashed-dotted lines in Fig. 5, in addition to the numerical cross-slip stress predictions.

Fig. 5 shows the predicted cross-slip stress with concentration at different temperatures for the six softening elements K, Na, Sc, Ca, Y and Zr. The curves are for the numerical solution of the Orowan equation, with dashed lines for the analytic approximations for softening and athermal hardening. All six solutes—including the first three predicted in Ref. [11]—show softening for low concentrations which becomes hardening at higher concentrations; the range of solute concentration that leads to softening decreases at higher temperatures. These predictions suggest possible alloying concentrations that can lead to lower stress for thermally activated cross-slip, and hence decrease the plastic anisotropy. At 600 K, the cross-slip stress is 4.1 MPa from our model; that cross-slip stress occurs at 533 K for Mg–0.4 at.%K, 560 K for Mg–1.0 at.%Na, 562 K for Mg–0.9 at.%Sc, 513 K for Mg–0.3 at.%Ca, 487 K for Mg–0.3 at.%Y and 565 K for Mg–0.7 at.%Zr. The predicted softening for Mg–K, Mg–Na and Mg–Sc is similar to the direct interaction calculation in Ref. [11], though the concentrations are slightly different. This reduction in plastic anisotropy is also captured in the ratio of softening potency to athermal hardening, χ; larger χ suggests a larger possible reduction in forming temperature. We expect all six of these alloys to be formable below 300 °C, with Mg–Y showing the lowest forming temperature. Note that studies of Mg–Y alloys at elevated temperatures (550 K) show increased non-basal dislocation activity [24].

Alloying Mg with Li is difficult to capture accurately with our model due to the weak interaction; but is consistent with experimental data on softening [6]. The average interaction energy predicted is nearly zero, and

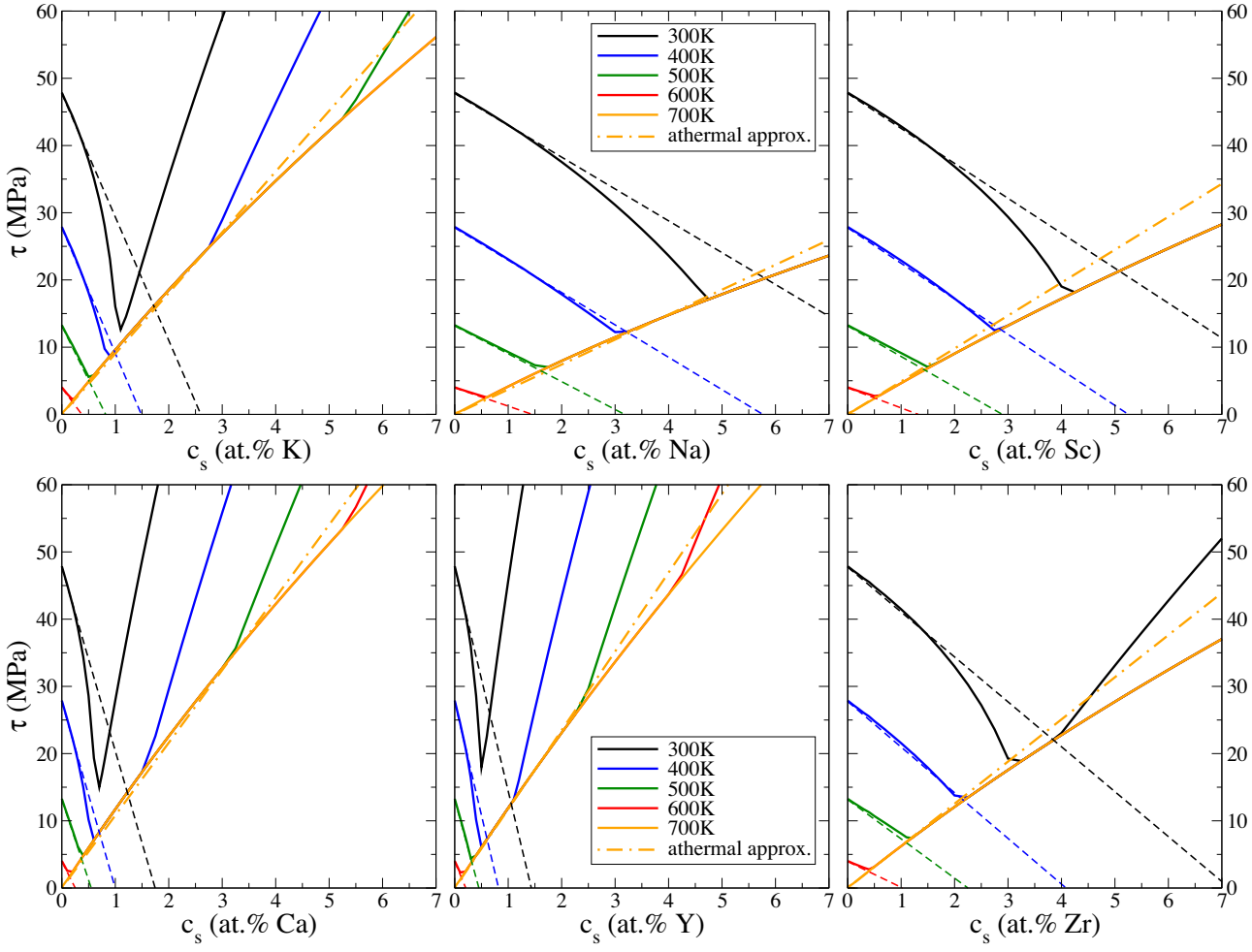

Fig. 5. Cross-slip stress with concentration for K, Na, Sc, Ca, Y and Zr from 300–700 K. Increasing temperature lowers the pure Mg cross-slip stress; small additions of attractive solutes increase the double-kink nucleation rate, leading to softening. The lower bound on all of these curves is the athermal stress $\tau^a(c_s)$. The dashed lines show the linear softening analytic approximation, and the dashed-dotted curves are the linear analytic approximation to the athermal stress. All of these cases show a minimum cross-slip stress for a given temperature. The first three solutes were previously predicted from direct interaction energy calculations [11], and compare well; the last three solutes require the geometric interaction model to predict solute–dislocation interactions.

the standard deviation is 13 meV; unfortunately, this is the same size as the prediction error. Li has the weakest interaction, and is also unusual in that it can produce softening of cross-slip without reducing the prismatic stacking fault energy. In this case, Li increases the basal stacking fault energy significantly more, and so can still reduce the kink formation energy. The predicted $P_{dk} = 0.7$ would be higher if the site energies are more attractive. We can estimate a range of possible P_{dk} (and $\tau_{ath}/\tau^{\star}$) by assuming that the errors in four unique site energies are independent and normally distributed with width 14 meV. If the average site energy was lowered to -14 meV (from 0 meV) and the standard deviation increased to $(13.2^2 + 14^2) = 19.2$ meV, then the softening potency is $P_{dk} = 9.1$. Experimental measurements of Mg–7.9 at.%Li show a reduction in cross-slip stress that is roughly one-half of the pure Mg cross-slip stress [6]; this corresponds, in the analytic model, to $P_{dk} = 8.9$. Therefore, while our model is not accurate enough to predict the exact softening potency of Li, our calculations do not contradict the known softening of Li. It is worth noting that $c_s = 0.079$ is a "high" concentration for the analytic softening model, and the numerical softening curves in Fig. 5 curve down, suggesting that a weaker interaction energy might still give the requisite softening. The subject of Mg–Li interactions remains a worthy problem for future study to predict cross-slip stress for Mg–Li alloys.

Finally, note that several solutes have negative misfits while $\varepsilon_{E1} > 0$, and do produce attractive site energies, but not of sufficient magnitude to induce softening. Table 1 includes many solutes with negative ε_{E2}, ε_{H1} or ε_{H2}, while ε_{E1} remains positive. Of these, As, Bi, Ge, Pb, Sb, Si and Tl are attractive to a prismatic screw dislocation core at sites $2t$ and 2ℓ; and Bi and Pb are attractive at $4t$ and 4ℓ. However, these attractive interactions do not lead to softening due to the simultaneous attractive interaction at the basal screw dislocation core site; hence, the overall interaction is positive. In addition, the other prismatic core sites remain repulsive. This further supports the general conclusion that ε_{E1} is the most important interaction to cause softening, possibly combined with a repulsive interaction for the basal screw dislocation core.

4. Conclusions

Our geometric model of solute interaction in a prismatic screw dislocation core combined with our previous computational model of basal to prismatic cross-slip above room temperature [11] and our geometric model of solute interactions with basal dislocations [16] have allowed us to efficiently calculate and predict cross-slip softening and hardening for 29 Mg binary alloys. From our interaction data, we predict six binary Mg alloys which soften prismatic slip—Ca, K, Na, Sc, Y and Zr—and suggest that Mg–Li alloys could also have lower cross-slip stress above room temperature and be formable below 300 °C. We connect the softening of thermal cross-slip primarily to a reduction in the easy prismatic stacking fault energy, though other combinations are possible. Our quantitative model can be used to predict the change in prismatic cross-slip stress for other solute elements, and this general approach—from dislocation core geometry predictions to interaction energy calculation to kink nucleation thermodynamics—can be applied to other systems with thermally activated slip. We also hope that these predictions lead to new experimental measurements of cross-slip stress at elevated temperatures in Mg alloys to provide additional validation of our predictions.

Acknowledgments

This research was sponsored by NSF through the GOALI program, Grant 0825961, and with the support of General Motors, LLC; in part by NSF through TeraGrid resources provided by NCSA and TACC; the Turing cluster maintained and operated by the Computational Science and Engineering Program at the Univ. Illinois; with a donation from Intel; and computational resources, networking, and support provided by GM Information Systems and Services. Fig. 1 was rendered with VMD [25].

References

[1] Pollock TM. Science 2010;328(5981):986–7. doi:10.1126/science.1182848.
[2] Friedrich HE, Mordike BL. Magnesium technology: metallurgy, design data, applications. Berlin: Springer; 2006.
[3] Taylor GI. J Inst Metals 1938;62:307–38.
[4] Agnew SR, Duygulua Ö. Int J Plast 2005;21:1161–93. doi:10.1016/j.ijplas.2004.05.018.
[5] Akhtar A, Teghtsoonian E. Acta Metall 1969;17:1351–6.
[6] Ahmadieh A, Mitchell J, Dorn JE. Trans Met Soc AIME 1965;233:1130–7.
[7] Urakami A, Meshii M, Fine ME. Acta Metall 1970;18:87–99.
[8] Urakami A, Meshii M, Fine ME. Proc 2nd ICMSA 1970;1:272–6.
[9] Urakami A, Fine ME. Acta Metall 1971;19:887–94.
[10] Pink E, Arsenault RJ. Prog Mater Sci 1979;24:1–50.
[11] Yasi JA, Hector Jr LG, Trinkle DR. Acta Mater 2011;59:5652–60. doi:10.1016/j.actamat.2011.05.040.
[12] Couret A, Caillard D. Acta Metall 1985;33:1447–54.
[13] Couret A, Caillard D. Acta Metall 1985;33:1455–61.
[14] Couret A, Caillard D, Püschl W, Schoeck G. Philos Mag A 1991;63:1045–57.
[15] Ward Flynn PW, Mote J, Dorn JE. Trans Metall Soc AIME 1961;221:1148–54.
[16] Yasi JA, Hector Jr LG, Trinkle DR. Acta Mater 2010;58:5704–13. doi:10.1016/j.actamat.2010.06.045.
[17] Kresse G, Hafner J. Phys Rev B 1993;47(1):RC558–?>RC561.
[18] Kresse G, Furthmüller J. Phys Rev B 1996;54(16):11169–86.
[19] Blöchl PE. Phys Rev B 1994;50:17953–9979.
[20] Kresse G, Joubert D. Phys Rev B 1999;59:1758–75.
[21] Perdew JP, Wang Y. Phys Rev B 1992;45(23):13244–9.
[22] Sun DY, Mendelev MI, Becker CA, Kudin K, Haxhimali T, Asta M, et al. Phys Rev B 2006;73:024116. doi:10.1103/PhysRevB.73.024116.
[23] Yasi JA, Nogaret T, Trinkle DR, Qi Y, Hector Jr LG, Curtin WA. Model Simul Mater Sci Eng 2009;17:055012. doi:10.1088/0965-0393/17/5/055012.
[24] Suzuki M, Sato H, Maruyama K, Oikawa H. Mater Sci Eng A 1998;252(2):248–55. doi:10.1016/S0921-5093(98)00662-5.
[25] Humphrey W, Dalke A, Schulten K. J Mol Graphics 1996;14:33–8.